

# Computing the gradients with respect to all parameters of a quantum neural network using a single circuit

Guang Ping He

School of Physics, Sun Yat-sen University, Guangzhou 510275, China

**Finding gradients is a crucial step in training machine learning models. For quantum neural networks, computing gradients using the parameter-shift rule requires calculating the cost function twice for each adjustable parameter in the network. When the total number of parameters is large, the quantum circuit must be repeatedly adjusted and executed, leading to significant computational overhead. Here we propose an approach to compute all gradients using a single circuit only, significantly reducing both the circuit depth and the number of classical registers required. We experimentally validate our approach on both quantum simulators and IBM’s real quantum hardware, demonstrating that our method significantly reduces circuit compilation time compared to the conventional approach, resulting in a substantial speedup in total runtime.**

## 1 Introduction

Artificial intelligence technology is making incredible progress nowadays. One of the main reasons is that classical artificial neural networks are made very feasible with the advance of computer science in recent years. On the other hand, though it is widely believed that quantum neural networks may breathe new life into the researches [1], they are still not as practical as their classical counterparts due to the scale and performance of currently available quantum computers. Especially, highly effective methods have been developed for computing the gradients of the cost function with respect to the adjustable parameters of classical neural networks, e.g., the back-propagation algorithm [2, 3]. A distinct feature

is that the cost function needs to be calculated only once, and all the gradients will be readily deduced, so that classical neural networks can be trained fast and efficiently. But for quantum neural networks, computing the gradients is considerably less convenient [4]. Effective algorithms were found for certain network architectures only [5]. For other general architectures, the parameter-shift rule [6, 7] seems to be the best algorithm found for this task so far. But it needs to calculate the cost function twice for computing the gradient with respect to a single parameter of the network (which will be further elaborated below). The values of some parameters for each calculation need adjustment too. Consequently, the quantum circuit for calculating the cost function has to be modified many times in order to obtain the gradients with respect to all parameters in each single round of training of the quantum network.

In this paper, we will propose an approach in which the gradients with respect to all parameters of a quantum neural network can be computed simultaneously using a single circuit only. The main purpose is to break the limit on the scale of computation on real quantum hardware. As it is well-known, the number of adjustable parameters of a powerful neural network is generally very high. If we have to run two quantum circuits to compute the gradient with respect to a single parameter, then the total number of unique executed circuits could easily exceed the capacity of any real quantum computer in existence. Of course, the execution of these circuits can be broken down into many “jobs”. But it is obviously inconvenient when we are using quantum cloud computation platforms. Especially, if the jobs are submitted separately, then there could be a long waiting time between the execution of the jobs. For example, for free users on the IBM Quantum Experience online platform, this

Guang Ping He: [hegp@mail.sysu.edu.cn](mailto:hegp@mail.sysu.edu.cn)

arXiv:2307.08167v4 [quant-ph] 30 Jan 2025

waiting time could vary from 10 minutes to 4 hours. For paying users, as also pointed out in Ref. [7], “quantum hardware devices are typically billed and queued per unique circuit”. According to Amazon Braket, the quantum computation platforms Rigetti, IonQ, OQC, and Quera all charge \$0.3 USD per unique circuit in addition to other fees [8]. A conventional method for reducing the number of unique circuits is to “stack” many circuits into a single job. In the Qiskit software development kit for running IBM quantum computers and simulators with Python programs, this can be done using the “append” function [9]. But there is also a restriction on its usage on real quantum computers. For example, on the “ibmq\_quito” backend, the number of circuits allowed to be appended is limited to 100. To break this limit, the Qiskit’s “compose” function can serve as an alternative. According to our experience, it runs much slower than the “append” method does. On platforms that charge by the runtime, slower programs mean higher cost. As of now, the rate in IBM Cloud’s Pay-As-You-Go Plan is \$96 USD per minute [10]. Nevertheless, it can indeed stack more circuits into one single job so that the gradients with respect to more parameters can be computed together.

In the following, we will use the direct stacking method based on the “compose” function (referred to as the “conventional approach”) as a baseline to compare with the performance of our proposed method that uses a single circuit only (referred to as the “improved approach”). In the next section, we will briefly introduce the typical structure of quantum neural networks. The parameter-shift rule will be reviewed in Section 3. Subsequently, our improved approach will be presented in Section 4, with its theoretical advantages — namely, reduced circuit depth and lower classical memory requirements — elaborated in Section 5. However, this approach also carries some theoretical disadvantages: the circuit needs two additional qubits, and requires more shots to run compared to the conventional approach, as explained in Section 6. To demonstrate that the advantages outweigh these disadvantages, we conduct experiments, and the results are reported in Section 7. These results show a significant speedup in total runtime, particularly as the number of input data points and the scale of the quantum circuit increase. Fi-

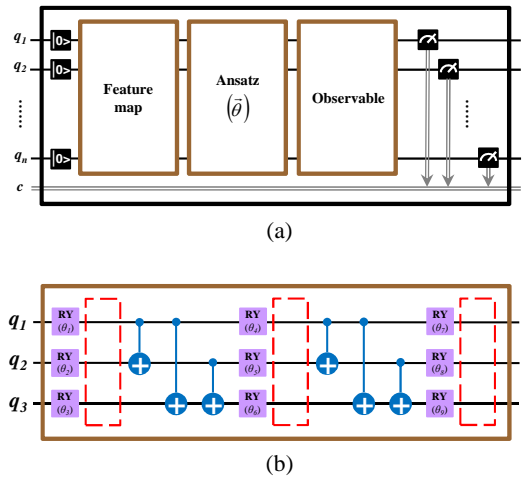


Figure 1: (a) The general structure of a variational quantum circuit (VQC). All qubits  $q_i$  ( $i = 1, \dots, n$ ) are initialized in the state  $|0\rangle$ , then pass through three blocks: the feature map, the ansatz and the observable, which apply certain unitary transformations. Finally they are measured in the computational basis, and the result is sent to the classical register  $c$ . All the adjustable parameters  $\vec{\theta} = (\theta_1, \dots, \theta_n)$  are contained in the ansatz. (b) An example of the *RealAmplitudes* ansatz on three qubits, with two repetitions and full entanglement.  $R_Y(\theta_i)$  ( $i = 1, \dots, 9$ ) are single-qubit  $R_Y$  rotation gates, with the adjustable parameter  $\theta_i$  denoting the rotation angle about the  $y$ -axis. The blue icons are CX (controlled-NOT) gates. The red dashed boxes denote where the additional circuit of our improved approach shown in Fig.3 will be added.

nally, in Section 8, we discuss the generalization of our approach, and suggest some improvements on real quantum hardware which can make our approach even faster.

## 2 The variational quantum circuit

There are various types of quantum neural networks. Among them, variational quantum circuits (VQCs) [11, 12, 13, 14, 15, 16, 17, 18] have the advantage that it can be implemented on current or near-term noisy intermediate-scale quantum computers, as demonstrated experimentally [19, 20, 21, 22]. Applications within this framework also include variational quantum simulators [23, 24], quantum approximate optimization algorithm [25, 26, 27], et al. Research domains extend across high-energy physics [28, 29], cybersecurity [30, 31], and finance [32, 33]. In this paper, we will use VQCs as an example to illustrate how our improved approach can be applied to compute the

gradients with respect to their parameters.

As shown in Fig.1(a), the general structure of a VQC can be divided into three blocks: the feature map, the ansatz, and the measurement of the observable, which gives the value of the cost function. Note that the goal of this paper is to provide a method for computing the gradients, instead of finding a VQC for a specific application. To this end, the details of the feature map and the measurement are less relevant, and our approach does not need to modify them. Thus, we will leave their description in the Experiments section. The ansatz is the most important block, because it contains all the adjustable parameters with respect to whom the gradients need to be computed. Our example uses the *RealAmplitudes* ansatz [34], which is the default ansatz in Qiskit’s VQC implementation. As pointed out in Ref. [17], this ansatz has also been used in a VQC with proven advantages over traditional feedforward neural networks in terms of both capacity and trainability [16]. The typical structure of the *RealAmplitudes* ansatz is illustrated in Fig.1(b).

### 3 The parameter-shift rule

Finding the gradients is a must for optimizing neural networks for certain applications. In our example, the original parameter-shift rule proposed in Ref. [6] will be used, where the exact gradient of the cost function  $f = f(\vec{\theta})$  with respect to the parameters  $\vec{\theta} = (\theta_1, \dots, \theta_n)$  of the quantum gates is obtained as

$$\frac{\partial f}{\partial \theta_i} = r \left( f(\vec{\theta} + s\vec{e}_i) - f(\vec{\theta} - s\vec{e}_i) \right) \quad (1)$$

for  $i = 1, \dots, n$ , where  $r = 1/2$  and  $s = \pi/2$  for all the rotation and phase gates available in the Qiskit library.

This equation shows that computing the gradient with respect to a single parameter  $\theta_i$  needs to calculate the cost function  $f$  twice, each time with a different set of parameters, i.e.,  $\vec{\theta} + s\vec{e}_i = (\theta_1, \dots, \theta_i + s, \dots, \theta_n)$  and  $\vec{\theta} - s\vec{e}_i = (\theta_1, \dots, \theta_i - s, \dots, \theta_n)$ . Therefore, when the total number of parameters of a VQC is  $n$ , computing all the gradients will have to run  $2n$  circuits with different values of the parameters. To stack these circuits into a single job, the aforementioned conventional approach is simply to connect them one after another using Qiskit’s “compose” function,

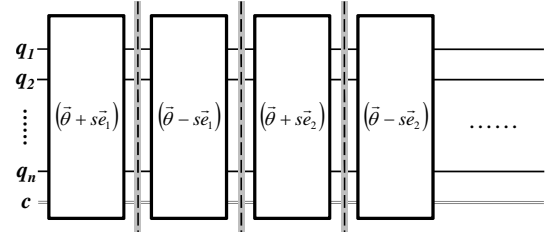


Figure 2: Diagram of the conventional approach, in which the circuits of many VQCs are stacked in serial using Qiskit’s “compose” function. Each black box contains all the components of the complete VQC shown in Fig.1(a), i.e., the feature map, the ansatz, and the observable along with the measurement. But the adjustable parameters  $\vec{\theta} = (\theta_1, \dots, \theta_n)$  for each ansatz take different values.

as illustrated in Fig.2. Each circuit is independently executed and measured before the next one is re-initialized and parameterized with new values, and the measurement results are stored in different classical registers.

### 4 Our improved approach

Now it will be shown how to compute all the  $2n$  shifted cost functions as well as the original unshifted cost function  $f(\vec{\theta})$  using a single circuit. The main idea is to introduce additional gates for realizing the shifts to the existing parameterized gates of the ansatz. Each of these additional gates is activated with a certain probability, so that each shift stands a chance to take effect. When none of these gates activate, the circuit acts exactly like the original ansatz so that the unshifted cost function will be computed. The key part is to ensure that these gates will be activated only one at a time at the most. That is, in each run (i.e., “shot”) of the circuit, there should not be two (or more) additional gates activate simultaneously. Otherwise, the circuit will output the cost function with the form like  $f(\vec{\theta} + s\vec{e}_i + s\vec{e}_j)$  ( $i \neq j$ ) which could be useful for calculating higher-order derivatives but is useless for computing the gradient via Eq. (1), while significantly lowers the efficiency of the circuit.

For this purpose, we add two additional control qubits  $q_a$  and  $q_b$  to the circuit, regardless the number of qubits and parameters in the original ansatz. Then for each existing single-parameter rotation gate  $RY(\theta_i)$  ( $i = 1, \dots, n$ ), we added

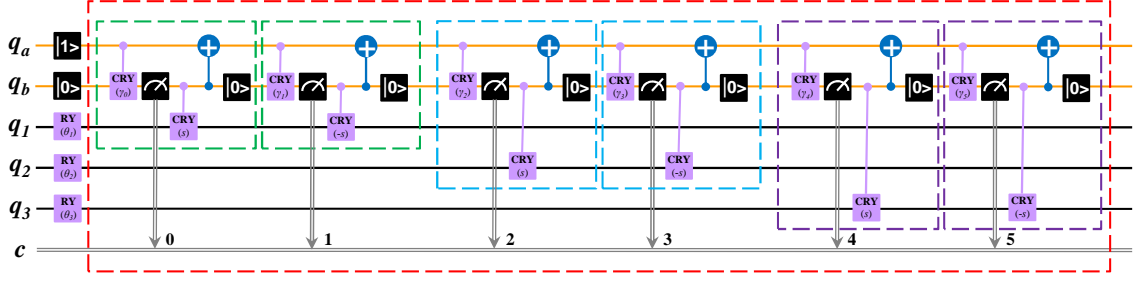


Figure 3: The quantum circuit for our improve approach. The section inside the red dashed box can be put into any one of the three red dashed boxes in Fig.1(b). Here  $q_a$  and  $q_b$  are the additional control qubits. They need to be initialized in the states  $|1\rangle_{q_a}$  and  $|0\rangle_{q_b}$  only once at the very beginning of Fig.1(b). The two green/blue/purple dashed boxes will create the shift  $\pm s$  to the gates  $RY(\theta_1)/RY(\theta_2)/RY(\theta_3)$ , respectively, with equal probabilities as controlled by  $q_a$  and  $q_b$ . Each of these dashed boxes starts with a controlled-RY gate  $CRY(\gamma_j)$ , where  $\gamma_j$  is defined in Eq. (8). Then a measurement is made on  $q_b$ , with the result recorded in the classical registers. Another controlled-RY gate  $CRY(\pm s)$  is placed between  $q_b$  and  $q_i$  ( $i = 1, 2, 3$ ), followed by a CX gate between  $q_b$  and  $q_a$ . Finally,  $q_b$  is reset to the state  $|0\rangle_{q_b}$ .

two blocks acting on the qubit it rotates and the above two additional control qubits, to turn the parameter from  $\theta_i$  to  $\theta_i + s$  and  $\theta_i - s$ , respectively. Each block contains 2 controlled-RY gates, 1 CX (two-qubit controlled-NOT) gate, 1 measurement and 1 reset operation. Fig.3 showcases an example of the resultant circuit. For simplicity, only three RY gates in the *RealAmplitudes* ansatz of the original VQC (corresponding to the three RY gates before any of the red dashed boxes in Fig.1(b)) are studied, and shown with the two additional blocks added to each of them. We also uploaded the diagram of the complete quantum circuit for a VQC with 10 qubits (which will be used in the Experiments section for the classification task of the MNIST dataset) to Github (available at: [https://github.com/gphehub/grad2210/blob/main/Fig.7\\_Complete\\_circuit\\_for\\_MNIST\\_classification.emf](https://github.com/gphehub/grad2210/blob/main/Fig.7_Complete_circuit_for_MNIST_classification.emf)).

Let us track the circuit in Fig.3 from left to right to see how it works. The role of the first additional control qubit  $q_a$  is to record whether any of the additional blocks has been activated. It can also be considered as a switch. If it is in the state  $|\psi\rangle_{q_a} = |1\rangle_{q_a}$ , then it means that no block has ever been activated yet. Or if it is flipped to the state  $|\psi\rangle_{q_a} = |0\rangle_{q_a}$ , then it implies that one of the blocks was already activated. The second additional control qubit  $q_b$  acts like a quantum dice, which controls the probability for each block to be activated. At the very beginning of the whole VQC,  $q_a$  and  $q_b$  are initialized in the states  $|1\rangle_{q_a}$  and  $|0\rangle_{q_b}$ , respectively.

Next, in the first green block right behind the first RY gate  $RY(\theta_1)$ , the first gate  $CRY(\gamma_0)$  is a controlled-RY gate with  $q_a$  ( $q_b$ ) serving as the control (target) qubit. It introduces a rotation angle

$$\gamma_0 = 2 \arcsin \sqrt{\frac{1}{N-0}} \quad (2)$$

about the  $y$ -axis to  $q_b$  only when  $|\psi\rangle_{q_a} = |1\rangle_{q_a}$ . Here  $N = 2n + 1$ . Then the state of  $q_b$  becomes

$$\begin{aligned} |\psi\rangle_{q_b} &= \cos \frac{\gamma_0}{2} |0\rangle_{q_b} + \sin \frac{\gamma_0}{2} |1\rangle_{q_b} \\ &= \sqrt{1 - \frac{1}{N-0}} |0\rangle_{q_b} + \sqrt{\frac{1}{N-0}} |1\rangle_{q_b} \end{aligned} \quad (3)$$

A measurement in the computational basis  $\{|0\rangle, |1\rangle\}$  is then made on  $q_b$ , and the result is sent to a classical register. With probability  $1/N$  the measurement result will be  $|1\rangle_{q_b}$ . In this case, the controlled-RY gate  $CRY(s)$  next to the measurement will be activated, introducing a rotation angle  $s = \pi/2$  to  $q_1$  (i.e., the qubit on which the gate  $RY(\theta_1)$  of the original ansatz is applied). Since the RY gates has the property

$$RY(s)RY(\theta_1) = RY(\theta_1 + s), \quad (4)$$

we can see that a shift  $s$  is successfully introduced to the parameter  $\theta_1$ . Meanwhile, with the next CX gate where  $q_b$  ( $q_a$ ) serves as the control (target) qubit, the state of  $q_a$  is turned from  $|1\rangle_{q_a}$  into  $|0\rangle_{q_a}$ , indicating that the current block was activated. Also, at the end of this block, the state of  $q_b$  is reset to  $|0\rangle_{q_b}$  regardless the measurement

result. Consequently, all the rest blocks that follows will be bypassed. After executing the entire circuit, the final result will give the cost function  $f(\vec{\theta} + s\vec{e}_1)$ .

On the other hand, with probability  $1 - (1/N)$  the measurement result on  $q_b$  in this block will be  $|0\rangle_{q_b}$ , as indicated by Eq. (3). Then the two aforementioned controlled gates in the same block following this measurement will not take effect at all, so that the states of  $q_a$  and  $q_1$  remain unchanged, allowing the second green block to be activated.

Similarly, in the second green block, since the state of  $q_b$  was reset to  $|0\rangle_{q_b}$ , the first gate  $CRY(\gamma_1)$  introduces a rotation angle

$$\gamma_1 = 2 \arcsin \sqrt{\frac{1}{N-1}} \quad (5)$$

to  $q_b$  when  $|\psi\rangle_{q_a} = |1\rangle_{q_a}$ , turning the state of  $q_b$  into

$$\begin{aligned} |\psi\rangle_{q_b} &= \cos \frac{\gamma_1}{2} |0\rangle_{q_b} + \sin \frac{\gamma_1}{2} |1\rangle_{q_b} \\ &= \sqrt{1 - \frac{1}{N-1}} |0\rangle_{q_b} + \sqrt{\frac{1}{N-1}} |1\rangle_{q_b} \end{aligned} \quad (6)$$

Then  $q_b$  is also measured in the computational basis, and the result is stored in another classical register. With probability  $1/(N-1)$  the result will be  $|1\rangle_{q_b}$ . Note that this case occurs only when the first block was not activated, i.e., the measurement result of  $q_b$  in the first block was  $|0\rangle_{q_b}$ , which occurred with probability  $1 - (1/N)$ . Thus, the total probability for finding  $q_b$  in  $|1\rangle_{q_b}$  at this stage (i.e., the second block is activated) is

$$prob_2 = \left(1 - \frac{1}{N}\right) \frac{1}{N-1} = \frac{1}{N}, \quad (7)$$

which equals to the probability for activating the first block. When this result indeed occurs, the next gate  $CRY(-s)$  will introduce the rotation angle  $-s = -\pi/2$  to  $q_1$ , and the CX gate next to it will turn the state of  $q_a$  into  $|0\rangle_{q_a}$ , making the rest blocks bypassed. Then the final result of the entire circuit will be the cost function  $f(\vec{\theta} - s\vec{e}_1)$ .

For the same reasons, by setting the rotation angle of the first controlled-RY gate  $CRY(\gamma_j)$  in the  $(j+1)$ th additional block as

$$\gamma_j = 2 \arcsin \sqrt{\frac{1}{N-j}} \quad (8)$$

( $j = 0, \dots, N-2$ ), it can be proven that every block stands the same probability  $1/N$  to be activated. The CX gates on  $q_b$  and  $q_a$  also ensure that only one block at the most will be activated. As a result, executing the whole circuit for one shot will give the output corresponding to the shifted cost function  $f(\vec{\theta} + s\vec{e}_j)$  or  $f(\vec{\theta} - s\vec{e}_j)$  for a single  $j$  only. When none of the block was activated (which also occurs with probability  $1/N$ ), the circuit outputs the unshifted cost function  $f(\vec{\theta})$ . By reading the classical registers  $c$  that store the measurement results of  $q_b$  in every block to see which block was activated, we can learn which cost function was calculated. Running the circuit for many shots will then provide enough shots for each of these cost functions, so that all gradients in Eq. (1) can be obtained with the desired precision.

After finding the gradients, the standard training routine can be applied for optimizing the corresponding VQC. That is, the value of each adjustable parameter  $\theta_i$  can be updated as

$$\theta_i \rightarrow \theta'_i = \theta_i - \eta \frac{\partial f}{\partial \theta_i}, \quad (9)$$

where  $\eta$  is the learning rate chosen by the user. Then the VQC should be reconstructed by using  $\vec{\theta}' = (\theta'_1, \dots, \theta'_n)$  as the new adjustable parameters of the ansatz. This completes one epoch of training. Computing the gradients using the new VQC and repeating this updating procedure for many epochs will eventually minimize the unshifted cost function, which means that the VQC is optimized for the given task.

## 5 Theoretical advantages

### 5.1 Circuit depth

Comparing with the conventional approach, a significant advantage of our improved approach is that the depth of the entire circuit is reduced, as estimated below.

For each single input data, let  $\Lambda$  denote the depth of the circuit for calculating the cost function once using the conventional approach, and  $n$  denote the number of the adjustable parameters. Define

$$\lambda = \frac{\Lambda}{n}. \quad (10)$$

In many ansatz,  $\lambda$  remains non-trivial even for high  $n$  (which will be proven in Appendix A by

using the *RealAmplitudes* ansatz as an example). Recall that computing the gradient with respect to a single parameter using the parameter-shift rule needs to calculate the cost function twice. Thus, the total depth of the stacked circuit for computing all the  $n$  gradients and the unshifted cost function using the conventional approach is

$$D_{conv} = \Lambda(2n + 1) = \lambda n(2n + 1) \propto O(n^2). \quad (11)$$

On the other hand, when using our improved approach, from Fig.3 we can see that a total of 10 operations were added to each existing parameterized RY gate of the original ansatz. Therefore, to compute all the  $n$  gradients and the unshifted cost function, the total depth of our circuit is simply

$$D_{impr} = \Lambda + 10n = \lambda n + 10n \propto O(n). \quad (12)$$

This result shows that our improved approach has the advantage that it takes a lower circuit depth when the number of parameters  $n$  is high, and the improvement will be more significant with the increase of  $n$ .

## 5.2 Number of classical bits in the stacked circuits

In the conventional approach, for each single input data, running the circuit for calculating the cost function once (either shifted or unshifted) takes  $Q$  classical bits to store the final measurement result of the  $Q$  qubits. When all the  $2n + 1$  circuits for computing all the  $n$  gradients and the unshifted cost function are stacked together so that it can be submitted as a single job on the real hardware, the total number of required classical bits is

$$N_{conv} = Q(2n + 1). \quad (13)$$

In our improved approach, the  $Q$  qubits of the original ansatz are measured only once at the very end of the circuit. The additional qubit  $q_b$  is measured twice in the two additional blocks added to each of the  $n$  parameterized gates of the original ansatz, which takes  $2n$  classical bits to store the results. At the end of the circuit, both the additional qubits  $q_a$  and  $q_b$  do not need to be measured. But for simplicity, we added these two measurements in our code too (not shown in Fig.3), which may also serve as an additional

monitoring of the running of the circuit. Consequently, the total number of classical bits required in our approach is

$$N_{impr} = Q + 2n + 2, \quad (14)$$

which is smaller than that of the conventional approach since generally  $Q \geq 2$ . This is another advantage of our approach.

## 6 Theoretical disadvantages

Our improved approach requires two more qubits than the conventional approach. It is considerable on free quantum computation platforms, which generally offers a total of 5~6 qubits only. But on near-term quantum devices that could really play a role in practical applications, the number of qubits has to be much higher, so that taking two more qubits should not make much difference.

What really matters is that our approach takes more shots than the conventional approach does in order to compute the gradients up to approximately the same precision. This is because in the conventional approach, when the stacked circuit is executed for  $s$  shots, each of the shifted and unshifted cost functions is calculated for exactly  $s$  shots too. But in our approach, when executing the circuit once, only one of the cost functions is calculated, depending on which of the additional blocks was activated by chance. To ensure that each cost function will be calculated for approximately  $s$  shots, our circuit needs to be executed for about  $s' = s(2n + 1)$  shots in total. This surely increases the runtime of the program. But recall that our circuit has a lower depth, so that it takes less time to compile. Therefore, whether our approach can result in a speedup on the total runtime depends on the competition between these two factors, and will be studied experimentally below.

Also, in our approach whether an additional block will be activated is controlled by the measurement result of the qubit  $q_b$ , where quantum uncertainty takes effect. Consequently, executing the circuit for  $s' = s(2n + 1)$  shots does not mean that each cost function will be calculated for  $s$  shots exactly. Some statistical fluctuations are inevitable. Nevertheless, the relationship between the number of shots and the precision of the results is also statistical and subjected to quantum

uncertainty. A fluctuation of the precision cannot be avoided even if all individual shot numbers are strictly aligned to the same value. Thus, we do not see the need to take extra efforts trying to level off the individual shot numbers of all the cost functions so that they equal exactly to each other. (In fact, this can simply be accomplished by discarding the data of some of the shots. But like we said, it seems unnecessary so that our experiments do not include this treatment.)

## 7 Experiments

To compare the performance of our improved approach and the conventional one, we tested them experimentally on both real quantum hardware and simulator.

### 7.1 The input datasets

Two classical input datasets are used in our experiments. One of them is an 8-dimensional dataset that we generated, where each data point  $x$  contains 8 random numbers  $\{x_1, \dots, x_8\}$  uniformly distributed over the interval  $[0, 1)$ . The intention of using such a random dataset is to ensure that our experimental results could stand less chances to be biased by the structure of the dataset.

The other is the 784-dimensional Modified National Institute of Standards and Technology (MNIST) dataset [35], which is a widely-used resource for machine learning research [36]. It contains 70000 greyscale  $28 \times 28 = 784$  pixel images of handwritten digits 0~9.

### 7.2 The feature map

Our feature map uses the amplitude encoding method [37], where each  $d$ -dimensional classical input data point  $x = \{x_1, \dots, x_d\}$  is encoded as the amplitudes of a  $Q$ -qubit quantum state

$$|\Phi_x\rangle = C_{norm} \sum_{i=1}^d x_i |i\rangle. \quad (15)$$

Here  $d = 2^Q$ ,  $|i\rangle$  is the  $i$ th computational basis state, and  $C_{norm}$  is the normalization constant.

### 7.3 The cost function

Though the form of the cost function plays an important role on the overall performance of a

neural network, it is less relevant to the current work because our main goal is to test the runtime of the improved approach only, which depends solely on the structure of the ansatz. Therefore, the cost function of our networks (either using the improved approach or the conventional one) is simply taken as

$$Cost = \frac{1}{m} \sum_x |a - y(x)| \quad (16)$$

where  $m$  is the number of input data,  $a$  is the vector of outputs from the network when  $x$  is input, and  $y(x)$  is the desired output, i.e., the label of the input  $x$ , as contained in the MNIST dataset.

Like the MNIST dataset, we also give each data in our 8-dimensional input dataset a label, so that our program can serve as a classifier if needed. But since our current data are generated randomly, we simply label all data as “2” without actual meaning.

### 7.4 Results

The first experiment is to test the validity of our improved approach. It is performed on quantum simulator using a VQC with the 8-dimensional classical input data, which takes  $Q = 3$  qubits to encode when using the amplitude encoding method. The *RealAmplitudes* ansatz in this VQC contains 1 repetition with full entanglement. Thus, it has  $n = 6$  adjustable parameters. We first calculate the exact amplitude distribution of the output states numerically, and use the result of the gradients as reference. Then we run the conventional approach for  $s = 500$  shots. For comparison, our improved approach for the same VQC is run for  $s' = 500 \times (2n + 1) = 6500$  shots, so that each cost function could be calculated for about  $s = 500$  shots in average (for simplicity, in the following when we say that the average number of shots for our improved approach is  $s$ , we mean that the actual number of shots is  $s' = s(2n + 1)$ ). The numbers of input data are all taken to be  $m = 20$  in these experiments. The results of the gradients are shown in Table I.

From the results we can see that when the (average) number of shots is  $s = 500$ , both approaches result in similar precision when comparing with the exact values. (The precision for the gradient  $grad(\theta_2)$  with respect to the second adjustable parameter  $\theta_2$  is low for both approaches, probably because the point happens to meet the

Table 1: Precision comparison between the two approaches on the obtained value of the gradient  $grad(\theta_i)$  with respect to the adjustable parameter  $\theta_i$  ( $i = 1, \dots, 6$ ). The VQC takes 8-dimensional classical input data, with the *RealAmplitudes* ansatz containing  $r = 1$  repetition and full entanglement. The number of input data is  $m = 20$ . The exact values are calculated numerically. The experimental values of both approaches are obtained using quantum simulator by taking  $s = 500$ . The relative deviation  $\Delta$  is calculated as (experimental value - exact value) / exact value.

Gradient	Exact value	Conventional approach		Improved approach	
		Experimental value	$\Delta$	Experimental value	$\Delta$
$grad(\theta_1)$	0.1527	0.1589	0.0403	0.1573	0.0298
$grad(\theta_2)$	-0.0030	-0.0050	0.6667	0.0010	-1.3181
$grad(\theta_3)$	-0.2667	-0.2691	0.0088	-0.2702	0.0131
$grad(\theta_4)$	-0.0837	-0.0897	0.0711	-0.0841	0.0052
$grad(\theta_5)$	0.1074	0.1064	-0.0093	0.1034	-0.0369
$grad(\theta_6)$	-0.1813	-0.1755	-0.0323	-0.1800	-0.0073

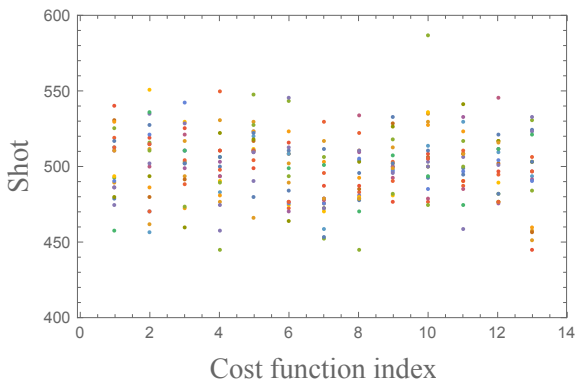


Figure 4: Individual number of shots actually computed for each cost function in our improved approach, corresponding to the experiment shown in the last column of Table 1. The average number of shots is taken to be  $s = 500$ . The number of input data is  $m = 20$ . The cost function with index 1 is the unshifted cost function, while the other 12 cost functions are all shifted ones. The dots with the same color represent the number of shots for the same input data point.

barren plateau [38, 39, 40, 41].) Thus, it is proven that the modified quantum circuit (i.e., Fig.3) in our improved approach works correctly as desired.

Secondly, we study the individual number of shots for each single cost function that was actually calculated in the above experiment using our improved approach. The result is shown in Fig.4. It is found that the fluctuation of the individual number of shots falls within the range [445, 587], with a standard deviation 22.6, which is only 4.52% of the average value  $s = 500$ , indicating that all the cost functions were calculated to almost the same precision.

Third and most importantly, the runtimes of both approaches are compared using 3 experiments:

Exp.1: The VQC used in Table I and Fig.4, run on quantum simulator.

Exp.2: The same VQC run on real quantum hardware (the “ibmq\_quito” backend).

Exp.3: A VQC with 784-dimensional classical input data, with the *RealAmplitudes* ansatz containing  $r = 2$  repetitions and full entanglement, run on quantum simulator. Note that this VQC takes  $Q = 10$  qubits to encode each input data with the amplitude encoding method, so that the total number of adjustable parameters is  $n = 30$  as given by Eq. (20).

Let  $t_c$  ( $t_r$ ) denote the time spent on compiling (running) the circuit. The sum  $t_s = t_c + t_r$  can serve as a good measure of the performance of the approaches, as the other parts of the computer programs (e.g., reading the input data and initial parameters, calculating the cost functions and gradients from the raw counting result of quantum simulator or real hardware, and exporting the results to the output files) run very fast and take almost the same amount of time for both approaches. The results are shown in Fig.5. The number of shots for each data point is fixed as  $s = 500$  (i.e., the actual number of shots is  $s' = 500(2n + 1)$  for our improved approach).

The following observations can be found in all these experiments.

(1) The values of  $t_r$  show that our improved approach always takes more time to run than the conventional approach does, either on simulator or real hardware. The difference is about

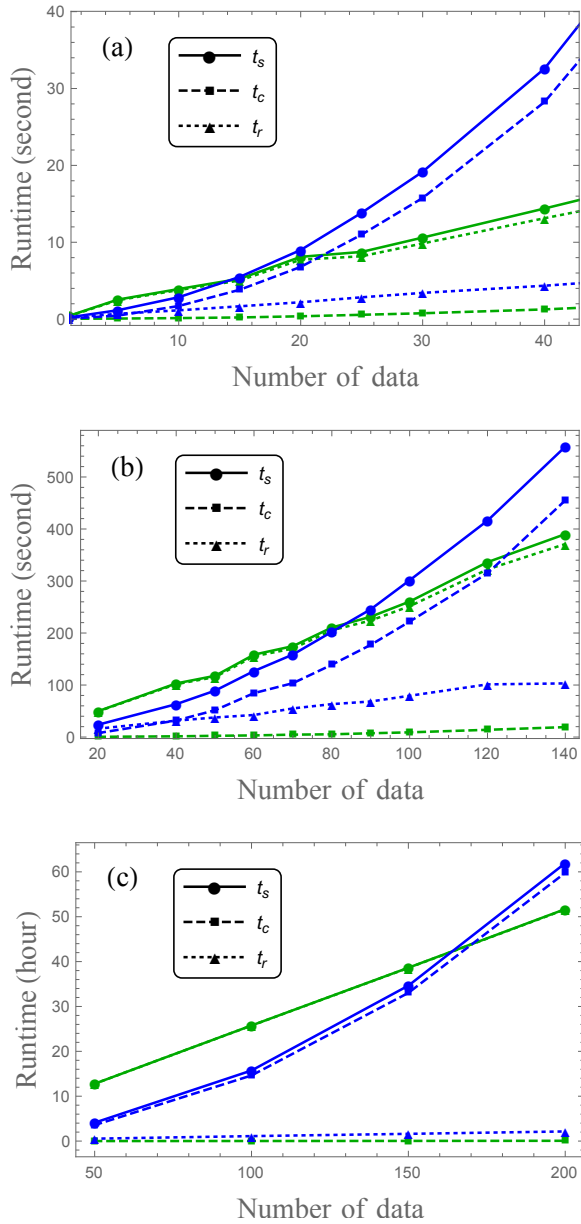


Figure 5: Runtimes as a function of the number of input data  $m$ . The dashed lines represent the time  $t_c$  spent on compiling the circuit, the dotted lines represent the time  $t_r$  spent on running the circuit, and the solid lines represent the total runtime  $t_s = t_c + t_r$ . All blue lines stand for the conventional approach, and all green lines stand for our improved approach. (a) Exp.1: The VQC used in the experiment in Fig.4, with 8-dimensional classical input data and the *RealAmplitudes* ansatz containing  $r = 1$  repetition and full entanglement, run on quantum simulator. (b) Exp.2: The same VQC as that of Exp.1, run on real quantum hardware. (c) Exp.3: A VQC with 784-dimensional classical input data, with the *RealAmplitudes* ansatz containing  $r = 2$  repetitions and full entanglement, run on quantum simulator. Note that the green solid and dotted lines almost overlap with each other since  $t_c \gg t_r$  so that  $t_s \simeq t_c$  for our improved approach in this case.

$3^4$  times (in Exp.1 and Exp.2) to 24 times (in Exp.3). This is not surprising, because the improved one needs to be run for more shots to reach the same precision.

(2) On the contrary, the values of  $t_c$  show that our improved approach saves a tremendous amount of time for compiling the circuit, which is only about 4% (in Exp.1 and Exp.2) to 0.1% (in Exp.3) of that of the conventional approach. This is owed to the significantly reduced circuit depth, as shown in Eq. (12).

(3) As the result of the competition between  $t_c$  and  $t_r$ , the total runtime  $t_s$  of the conventional approach is shorter when  $m$  (the number of input data) is low. But as  $m$  increases, our improved approach will eventually become faster. In Exp.1, the turning point occurs at around  $m = 15$  where both approaches take about 8 seconds to complete. After that,  $t_s$  of our approach increases approximately in a linear way, while  $t_s$  of the conventional one rises dramatically, mostly due to the long compiling time  $t_c$ . In both Exp.2 and Exp.3, the same behavior can be observed. The turning points occur relatively later though. This is because the real quantum hardware used in Exp.2 runs about  $10 \sim 30$  times slower than the simulator used in Exp.1, and Exp.3 has a more complicated circuit than that of Exp.1 though it is also run on simulator. Consequently, both Exp.2 and Exp.3 have a longer  $t_r$  than that of Exp.1. Meanwhile, all the three experiments have similar  $t_c$  values because the compiling of the circuits are always done on classical computers. Therefore, the slower the quantum hardware or simulator is, the later the turning point of the total runtime  $t_s$  occurs.

In the age of big data, for real applications of neural networks, the number of input data is generally much higher than what was used here. As a result, we can see that our improved approach has the advantage that it can save the total runtime. This advantage is expected to be even more obvious with the advance of real quantum computers, because they will surely run faster in the future than they do today, resulting in a shorter  $t_r$  so that the turning point of  $t_s$  could occur even earlier.

It is also worth noting that if Qiskit's "append" function were used for stacking the circuits, the "ibmq\_quito" real quantum backend only allows 100 circuits to be appended in a single job. Since

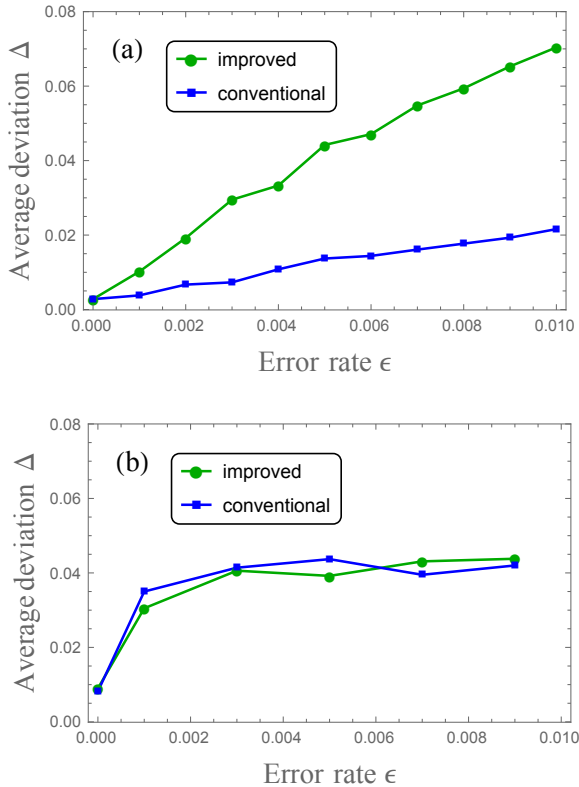


Figure 6: The average deviation  $\bar{\Delta}$  (as defined in Eq. (18)) of the cost functions as a function of  $\epsilon$ , which is the error rate of all quantum gates. The blue lines stand for the conventional approach, and the green lines stand for our improved approach. All data are computed using quantum simulator. (a) The same VQC used in Exp.1 of Fig.5(a), with 8-dimensional classical input data. The number of input data for each point in the figure is fixed as  $m = 20$ . (b) A VQC with 784-dimensional classical input data. The number of input data is  $m = 1$ . Both VQCs use the *RealAmplitudes* ansatz with  $r = 1$  repetitions and full entanglement.

the VQC in Exp.2 has 6 adjustable parameters, there are totally 13 shifted and unshifted cost functions to be calculated for each single input data. It means that using the “append” function can handle only  $m = \lfloor 100/13 \rfloor = 7$  input data at the most. But Exp.2 (i.e., Fig.5(b)) shows that both the conventional approach (using the “compose” function) and our improve approach can accomplish the computation for at least  $m = 140$  input data in a single job with no problem. Thus, they manage to break the limit on real quantum hardware.

Finally, the impact of noise in the circuits is studied and shown in Fig.6, where the value of the average deviation  $\bar{\Delta}$  is calculated as follows. The exact values  $f_i^{exa}$  ( $i = 1, \dots, 2n + 1$ ) of all the shifted and unshifted cost functions were cal-

culated numerically beforehand. Then the values  $f_i^{sim}$  of these cost functions are computed using the noise model in the simulator, where the error rate  $\epsilon$  of all quantum gates are taken to be equal for simplicity, and ranges from 0.001 to 0.01. The number of shots for each cost function is  $s = 1000$  (i.e.,  $s' = 1000(2n + 1)$  for our improved approach). Define

$$\Delta_i = \left| \frac{f_i^{sim} - f_i^{exa}}{f_i^{exa}} \right| \quad (17)$$

as the absolute value of the relative deviation between the results of the simulator and the exact values, and the average deviation is obtained as

$$\bar{\Delta} = \frac{1}{2n + 1} \sum_{i=1}^{2n+1} \Delta_i. \quad (18)$$

We first study the same VQC used in Exp.1 of Fig.5(a), which takes 8-dimensional classical input data, with the *RealAmplitudes* ansatz containing  $r = 1$  repetitions and full entanglement. The result is shown in Fig.6(a), where the number of input data is  $m = 20$ . We can see that the effect of noise in our improved approach is about 2~3 times more significant than that in the conventional approach. Theoretically, this is not unexpected, because it takes 3 qubits to encode 8-dimensional classical input data in the conventional approach, while our improved approach adds 2 more qubits to control the shifts to the parameterized gates. The same error rate surely brings more errors to 5 qubits than it does to 3 qubits. But we can expect that the difference should become less significant with higher-dimensional classical input data, which means an increase on the number of total qubits in the VQC. This is because in our improved approach, the number of additional qubits is always 2, regardless the number of qubits in the original VQC. Indeed, a VQC with 784-dimensional classical input data is studied in Fig.6(b). It is similar to the VQC in Exp.3 of Fig.5(c), but since the noise model in the simulator runs much slower than the noiseless one, here we only take  $r = 1$  repetition in the *RealAmplitudes* ansatz, so that the total number of adjustable parameters drops to  $n = 20$ . The number of input data is taken as  $m = 1$ . For 784-dimensional input, our improved approach takes 12 qubits in total, while the conventional approach takes 10 qubits.

The result in Fig.6(b) verifies the conjecture that the noise should display less difference between the two approaches when the number of qubits becomes close. In fact, when  $\epsilon = 0.001, 0.003$  and  $0.005$ , the average deviation of our improved approach is even slightly lower than that of the conventional approach (which is believed to be the consequence of the randomness in quantum simulation). The link to the source data of all figures is provided in the Data Availability section. More details of the computer programs and the environment is given in Appendix B.

## 8 Discussion

In summary, it is demonstrated experimentally that our improved approach manages to increase the number of gradients that can be computed in each single job, breaking the limit that can be reached using Qiskit’s “append” function. More importantly, it has a smaller circuit depth and requires less classical registers for storing the measurement results when comparing with the conventional approach using Qiskit’s “compose” function. This reduces the time spent for compiling the quantum circuit significantly. Therefore, the total runtime of the program can also be saved, especially when the number of input data is high and the structure of the quantum circuit is complicated.

Though we only demonstrated our improved approach for VQCs where each parameterized quantum gate  $U(\theta)$  satisfies

$$U(\theta + s) = U(\theta)U(s) \quad (19)$$

(i.e., the gates covered by the original parameter-shift rule [6]), it can also be modified to compute the gradients for any other quantum gate that requires the general parameter-shift rules [7]. For example, suppose that the first parameterized gate  $RY(\theta_1)$  on the qubit  $q_1$  in Fig.3 is replaced by a more general gate  $U'(\theta_1)$  that does not satisfy Eq. (19). To compute  $U'(\theta+s)$ , all we need is to replace the controlled-RY gate  $CRY(s)$  (controlled by  $q_b$  and acting on  $q_1$ ) in the first block right behind  $RY(\theta_1)$  in Fig.3 by two controlled-gates  $(U'(\theta_1))^{-1}$  and  $U'(\theta_1 + s)$  in serial, both of which are also controlled by  $q_b$  and acting on  $q_1$ . Here  $(U'(\theta_1))^{-1}$  is the reverse operation of  $U'(\theta_1)$  such that  $(U'(\theta_1))^{-1}U'(\theta_1) = I$ . We can see that once the measurement on  $q_b$  before them (i.e., the

measurement operator in the first block of Fig.3) results in  $|1\rangle_{q_b}$ , then these two gates will be activated. Combining with the original  $U'(\theta_1)$  gate, the complete operation on the qubit  $q_1$  will be  $U'(\theta_1 + s)(U'(\theta_1))^{-1}U'(\theta_1) = U'(\theta_1 + s)$ . Thus, the shift of such a general parameterized quantum gate can also be computed with our approach.

Our approach also suggests the following improvement on real quantum computers. From Fig.3 we can see that the purpose of the first two operations in each block (the controlled-RY gate  $CRY(\gamma_j)$  and the measurement) is to turn the state of  $q_b$  into  $|1\rangle_{q_b}$  with a certain probability. If there is a classical random number generator (even if it generates pseudorandom numbers only), it can accomplish the same task while further reducing the circuit depth. Also, the next two quantum controlled gates make use of the states  $|0\rangle$  and  $|1\rangle$  of  $q_a$  and  $q_b$  only, without needing their quantum superpositions. They can be replaced by classical IF gates (i.e., controlled gates that take classical control bits instead of control qubits, while the target registers can be either quantum or classical) and both  $q_a$  and  $q_b$  can be classical registers too, so that less quantum resource is required. Unfortunately, classical random number generator and the IF gate are currently unavailable on real quantum hardware (the latter is available on the simulator though). Our approach shows that there is the need for adding these operations in the future, so that the performance of real quantum computers for certain tasks can be further improved.

### Acknowledgments

This work was supported in part by Guangdong Basic and Applied Basic Research Foundation under Grant No. 2019A1515011048. The experiments in this work were supported in part by National Supercomputer Center in Guangzhou. The author thanks Qing Liu and the technical support team at National Supercomputer Center.

### Data Availability

The raw experimental data of this study are publicly available at <https://github.com/gphehub/grad2210>.

### Code Availability

The software codes for generating the experimental data are publicly available at <https://github.com/gphehub/grad2210>.

## References

- [1] Cerezo, M., Verdon, G., Huang, H. -Y., Cincio, L. & Coles, P. J. Challenges and opportunities in quantum machine learning. *Nat. Comput. Sci.* **2**, 567–576 (2022).
- [2] Rumelhart, D. E., Hinton, G. E. & Williams, R. J. Learning representations by back-propagating errors. *Nature* **323**, 533–536 (1986).
- [3] Nielson, M. A. *Neural networks and deep learning* (Determination Press, 2015).
- [4] Abbas, A., King, R., Huang, H. -Y., Huggins, W. J., Movassagh, R., Gilboa, D. & McClean, J. R. On quantum back-propagation, information reuse, and cheating measurement collapse. Preprint at <https://arxiv.org/abs/2305.13362> (2023).
- [5] Bowles, J., Wierichs, D. & Park, C. -Y. Backpropagation scaling in parameterised quantum circuits. Preprint at <https://arxiv.org/abs/2306.14962> (2023).
- [6] Schuld, M., Bergholm, V., Gogolin, C., Izaac, J. & Killoran, N. Evaluating analytic gradients on quantum hardware. *Phys. Rev. A* **99**, 032331 (2019).
- [7] Wierichs, D., Izaac, J., Wang, C. & Lin, C. Y. -Y. General parameter-shift rules for quantum gradients. *Quantum* **6**, 677 (2022).
- [8] Amazon braket, <https://aws.amazon.com/cn/braket/pricing> (Access on Jan. 30, 2025).
- [9] Games & Demos: Local reality and the CHSH inequality, in *Qiskit Textbook*. <https://learn.qiskit.org/course/ch-demos/local-reality-and-the-chsh-inequality> (Access on Jan. 30, 2023).
- [10] IBM cloud’s pay-as-you-go plan, <https://www.ibm.com/quantum/access-plans> (Access on Jan. 30, 2025).
- [11] Peruzzo, A., McClean, J., Shadbolt, P., Yung, M. -H., Zhou, X. -Q., Love, P. J., Aspuru-Guzik, A. & O’Brien, J. L. A variational eigenvalue solver on a photonic quantum processor. *Nat. Commun.* **5**, 4213 (2014).
- [12] Grant, E., Benedetti, M., Cao, S., Hallam, A., Lockhart, J., Stojevic, V., Green, A. G. & Severini, S. Hierarchical quantum classifiers. *npj Quantum Inf.* **4**, 65 (2018).
- [13] Benedetti, M., Lloyd, E., Sack, S. & Fiorentini, M. Parameterized quantum circuits as machine learning models. *Quantum Sci. Technol.* **4**(4), 043001 (2019).
- [14] LaRose, R. & Coyle, B. Robust data encodings for quantum classifiers. *Phys. Rev. A* **102**(3), 032420 (2020).
- [15] Cerezo, M., Arrasmith, A., Babbush, R., Benjamin, S. C., Endo, S., Fujii, K., McClean, J. R., Mitarai, K., Yuan, X., Cincio, L. & Coles, P. J. Variational quantum algorithms. *Nat. Rev. Phys.* **3**, 625–644 (2021).
- [16] Abbas, A., Sutter, D., Zoufal, C., Lucchi, A., Figalli, A. & Woerner, S. The power of quantum neural networks. *Nat. Comput. Sci.* **1**, 403–409 (2021).
- [17] Arthur, D. & Date, P. A hybrid quantum-classical neural network architecture for binary classification. Preprint at <https://arxiv.org/abs/2201.01820> (2022).
- [18] Du, Y., Huang, T., You, S., Hsieh, M. -H. & Tao, D. Quantum circuit architecture search for variational quantum algorithms. *npj Quantum Inf.* **8**, 62 (2022).
- [19] O’Malley, P. J. J., Babbush, R., Kivlichan, I. D., Romero, J., McClean, J. R., Barends, R., Kelly, J., Roushan, P., et al. Scalable quantum simulation of molecular energies. *Phys. Rev. X* **6**(3), 031007 (2016).
- [20] Kandala, A., Mezzacapo, A., Temme, K., Takita, M., Brink, M., Chow, J. M. & Gambetta, J. M. Hardware-efficient variational quantum eigensolver for small molecules and quantum magnets. *Nature* **549**, 242–246 (2017).
- [21] Cîrstoiu, C., Holmes, Z., Iosue, J., Cincio, L., Coles, P. J. & Sornborger, A. Variational fast forwarding for quantum simulation beyond the coherence time. *npj Quantum Inf.* **6**, 82 (2020).
- [22] Kim, Y., Eddins, A., Anand, S., Wei, K. X., van den Berg, E., Rosenblatt, S., Nayfeh, H., Wu, Y., Zaletel, M., Temme, K. & Kandala, A. Evidence for the utility of quantum computing before fault tolerance. *Nature* **618**, 500–505 (2023).
- [23] Li, Y. & Benjamin, S. C. Efficient variational quantum simulator incorporating active er-

- ror minimization. *Phys. Rev. X* **7**(2), 021050 (2017).
- [24] Endo, S., Sun, J., Li, Y., Benjamin, S. C. & Yuan, X. Variational quantum simulation of general processes. *Phys. Rev. Lett.* **125**(1), 010501 (2020).
- [25] Farhi, E., Goldstone, J. & Gutmann, S. A quantum approximate optimization algorithm. Preprint at <https://arxiv.org/abs/1411.4028> (2014).
- [26] Zhou, L., Wang, S. -T., Choi, S., Pichler, H. & Lukin, M. D. Quantum approximate optimization algorithm: Performance, mechanism, and implementation on near-term devices. *Phys. Rev. X* **10**(2), 021067 (2020).
- [27] Farhi, E., Goldstone, J., Gutmann, S. & Zhou, L. The quantum approximate optimization algorithm and the sherrington-kirkpatrick model at infinite size. *Quantum* **6**, 759 (2022).
- [28] Terashi, K., Kaneda, M., Kishimoto, T., Saito, M., Sawada, R. & Tanaka, J. Event classification with quantum machine learning in high-energy physics. *Comput. Softw. Big Sci.* **5**, 2 (2021).
- [29] Gianelle, A., Koppenburg, P., Lucchesi, D., Nicotra, D., Rodrigues, E., Sestini, L., de Vries, J. & Zuliani, D. Quantum machine learning for  $b$ -jet charge identification. *J. High Energ. Phys.* **2022**, 14 (2022).
- [30] Islam, M., Chowdhury, M., Khan, Z. & Khan, S. M. Hybrid quantum-classical neural network for cloud-supported in-vehicle cyberattack detection. *IEEE Sens. Lett.* **6**(4), 6001204 (2022).
- [31] Yusuf Küçükçkara, M., Atban, F. & Bayılmış C. Quantum-neural network model for platform independent DDos attack classification in cyber security. *Adv. Quantum Technol.* **7**(10), 2400084 (2024).
- [32] Emmanoulopoulos, D. & Dimoska, S. Quantum machine learning in finance: Time series forecasting. Preprint at <https://arxiv.org/abs/2202.00599> (2022).
- [33] Cherrat, E. A., Raj, S., Kerenidis, I., Shekhar, A., Wood, B., Dee, J., Chakrabarti, S., Chen, R., et al. Quantum deep hedging. *Quantum* **7**, 1191 (2023).
- [34] RealAmplitudes, in *Qiskit Documentation*. <https://qiskit.org/documentation/stubs/qiskit.circuit.library.RealAmplitudes.html> (Access on Oct. 6, 2022).
- [35] LeCun, Y. The MNIST database of handwritten digits. <http://yann.lecun.com/exdb/mnist/> (1998).
- [36] Deng, L. The MNIST database of handwritten digit images for machine learning research. *IEEE Signal Processing Magazine* **29**, 141–142 (2012).
- [37] LaRose, R. & Coyle, B. Robust data encodings for quantum classifiers. *Phys. Rev. A* **102**, 032420 (2020).
- [38] McClean, J. R., Boixo, S., Smelyanskiy, V. N., Babbush, R. & Neven, H. Barren plateaus in quantum neural network training landscapes. *Nat. Commun.* **9**, 4812 (2018).
- [39] Grant, E., Wossnig, L., Ostaszewski, M. & Benedetti, M. An initialization strategy for addressing barren plateaus in parametrized quantum circuits. *Quantum* **3**, 214 (2019).
- [40] Wang, S., Fontana, E., Cerezo, M., Sharma, K., Sone, A., Cincio, L. & Coles, P. J. Noise-induced barren plateaus in variational quantum algorithms. *Nat. Commun.* **12**, 6961 (2021).
- [41] Sack, S. H., Medina, R. A., Michailidis, A. A., Kueng, R. & Serbyn, M. Avoiding barren plateaus using classical shadows. *PRX Quantum* **3**(2), 020365 (2022).

## A Proving that $\lambda$ in Eq. (10) is non-trivial

In the *RealAmplitudes* ansatz, let  $Q$  denote the total number of the qubits. When  $Q$  is fixed, increasing  $n$  means increasing the number of repetition  $r$  in this ansatz. This is because the ansatz starts with a parameterized RY gate for each of the  $Q$  qubits, then each repetition adds another parameterized RY gate to each qubit. Thus, the total number of the parameters satisfies

$$n = Q(r + 1). \quad (20)$$

Suppose that the circuit depth of each additional repetition (including the RY gates and the CX

gates in the entanglement section) is  $\Delta$ . Then

$$\Lambda = \Lambda_0 + r\Delta = \Lambda_0 + \left(\frac{n}{Q} - 1\right)\Delta = (\Lambda_0 - \Delta) + n\frac{\Delta}{Q}, \quad (21)$$

where  $\Lambda_0$  denotes the depth of the other parts of the circuit which is not included in  $\Delta$ , e.g., the feature map, the observable, the final measurement, and the very first RY gate on each qubit within the ansatz. In this case, we yield

$$\lambda = \frac{(\Lambda_0 - \Delta) + n\frac{\Delta}{Q}}{n} = \frac{(\Lambda_0 - \Delta)}{n} + \frac{\Delta}{Q}. \quad (22)$$

A neural network that is useful in practice generally has a large number of parameters. When  $n \rightarrow \infty$  we have

$$\lim_{n \rightarrow \infty} \lambda = \Delta/Q. \quad (23)$$

Thus it is proven that  $\lambda$  stays non-trivial.

## B Program details

The programs for 8-dimensional input data using quantum simulator were run on a personal laptop with a 2.8 GHz quad-core Intel i7-3840QM processor and 16 GB 1,600 MHz DDR3 memory.

The programs for 784-dimensional input data using quantum simulator were run on a Tianhe-2 supercomputer node with a 2.2 GHz Intel Xeon E5-2692 v2 processor and 64 GB memory.

In these simulations, Qiskit’s “qasm\_simulator” backend was used as the quantum simulator.

The programs using real hardware were run on the “ibmq\_quito” 5-qubit backend of IBM Quantum Experience online platform.

The operating environment for all programs is Python 3.8.10 with Qiskit 0.21.2.

When running on quantum simulator, both  $t_c$  (the time spent on compiling the quantum circuit) and  $t_r$  (the time spent on running the circuit) are recorded automatically by the programs. But when running on real quantum hardware,  $t_r$  is obtained from the job output files downloaded from IBM Quantum Experience platform instead. This is because the value of  $t_r$  recorded by the programs in this case also includes the time spent on waiting in the queue for the job to be run, which is not the correct measure for the performance of the approaches being used.

In both approaches, the circuits for different input data are stacked together using Qiskit’s “compose” function.

The initial values of all adjustable parameters of the VQCs were generated randomly (uniformly distributed over the interval  $[0, \pi)$ ) and stored beforehand. Then we always loaded these same values into every computer programs in every run.

More details can be found in the file “file\_description.pdf” accompanies with the source codes (see Code Availability section).